



Supporting Online Material for  
**Leading-Edge Vortices Elevate Lift of Autorotating Plant Seeds**

D. Lentink,<sup>\*</sup> W. B. Dickson, J. L. van Leeuwen, M. H. Dickinson

<sup>\*</sup>To whom correspondence should be addressed. E-mail: [david.lentink@wur.nl](mailto:david.lentink@wur.nl)

Published 12 June 2009, *Science* **324**, 1438 (2009)  
DOI: 10.1126/science.1174196

**This PDF file includes:**

Materials and Methods  
Figs. S1 to S7  
Equations S1 to S7  
References

**Other Supporting Online Material for this manuscript includes the following:**  
(available at [www.sciencemag.org/cgi/content/full/324/5933/1438/DC1](http://www.sciencemag.org/cgi/content/full/324/5933/1438/DC1))

Movie S1

## Leading-Edge Vortices Elevate Lift of Autorotating Plant Seeds

D. Lentink<sup>1\*</sup>, W.B. Dickson<sup>2</sup>, J.L. van Leeuwen<sup>1</sup> and M.H. Dickinson<sup>2</sup>

<sup>1</sup>Experimental Zoology Group, Wageningen University, 6709 PG Wageningen, the Netherlands.

<sup>2</sup>Department of Bioengineering, California Institute of Technology, Pasadena, California 91125, USA.

\*To whom correspondence should be addressed. E-mail: david.lentink@wur.nl (D.L.)

page 2 **Methods**

page 4 **Movie S1. LEV visualization near the base of a freely flying *Acer pseudo-platanus* L.**

page 5 **Figure S1. Dynamically scaled Robot model of a descending autorotating seed**

page 6 **Figure S2. Stereo images of the LEV measured on seed models**

page 7 **Figure S3. Free flight LEV visualization setup based on a vertical wind tunnel.**

page 9 **Figure S4. LEV visualization near the base of 32 freely flying *Acer pseudo-platanus* L. seeds**

page 11 **Figure S5. Spanwise variation in cordwise flow of a freely flying *Acer pseudo-platanus* L.**

page 13 **Figure S6. Balsa wood models of *Acer pseudo-platanus* L.**

page 14 **Figure S7. Flow visualization at 30% span of *Acer pseudo-platanus* L. and various balsa models**

page 16 **Supplementary Equation. Relating descent time to wing loading and aerodynamic efficacy**

page 19 **References**

## Methods

**Dynamically-scaled robot seed.** Using a translating robotic arm immersed in a tank filled with mineral oil ( $S1$ ) (density =  $830 \text{ kg m}^{-3}$ ; kinematic viscosity =  $11.0 \times 10^{-6} \text{ m}^2 \text{ s}^{-1}$ ) we dynamically-scaled the kinematics of four model autorotating seeds (Fig. 1B) such that their planer shape, Reynolds number, and flight parameters (e.g. descent speed and angle of attack) matched those of freely flying seeds. The free flight parameters ( $S2$ ) and morphology ( $S2$ ;  $S3$ ) have been described previously. The angle of attack of the seeds was calculated based on the free flight data and by adding a negative pitch angle (close to  $-1^\circ$  at 75% radius) to the positive local geometric angle of attack (Fig. 1). The model wings were made from 1.5 mm thick transparent acrylic and had no twist, approximating the natural morphology of the flat seeds. (Fig. 1B). The distance between the wing's center of rotation and its tip was 130 mm for all model seeds to minimize wall effects, which we estimated to be within 1% of an infinite volume ( $S4$ ). We tilted the flight path  $90^\circ$  (horizontal) to enable the robot ( $S1$ ) to correctly translate and spin the seeds at their natural pitch and cone angle (Fig. 1A, Supplementary Fig.1).

**Stereo DPIV flow measurement.** We measured flow fields using the LaVision stereo DPIV software and hardware described in Poelma *et al.* ( $S5$ ). We collected data after the wings had spun two whole revolutions, at which point the flow was steady and repeatable. The pitch of the resulting tip vortex was large, such that interactions with tip vortices shed beyond one revolution can be assumed small (e.g. see Fig. 9 in Azuma and Yasuda ( $S2$ )). By repeating the DPIV measurements 10 times per spanwise section we were able to perform standard stereo ensemble correlation for every section (multipass:  $1 \times (64 \times 64)$  and  $2 \times (32 \times 32)$  each with 50% overlap) using DaVis 7.0, LaVision GmbH ( $S5$ ). We measured flow fields at 24 to 26 spanwise sections separated by 5 mm. Using custom Matlab software and Tecplot 360 we processed data and build up the three dimensional velocity field. The spanwise velocity field sampling proved to be smooth enough for plotting the lab frame streamlines as shown in Fig. 2 (view point & angle are identical in Fig. A-D, stereo angle offset is  $\pm 3.5$  degrees in online figure). To obtain high-quality vorticity fields we calculated the gradient of the flow field in the spanwise sections for which we had good resolution measurements. Through integration of the vorticity field in every spanwise section we obtained the corresponding spanwise circulation. For this we used a vorticity cut-off value 5% higher than the highest vorticity noise found in the upstream flow field in each particular spanwise section. We then used circulation to calculate section lift from the product of fluid density,  $\rho$ , sectional wing speed,  $U$ ,

and net sectional circulation. Finally, we calculated the sectional lift coefficient by dividing sectional lift by the product of sectional dynamic pressure ( $\frac{1}{2} \rho U^2$ ) and sectional chord length.

**Free flight experiments in air.** We built a vertical wind tunnel to test if real maple seeds (*Acer pseudo-platanus* L.) generate a LEV as predicted by our experiments with dynamically scaled models. The design was based on the vertical wind tunnel design of Yasuda and Azuma (S3). We generated smoke particles with a smoke generator (HQ POWER VDP900HZ), which we illuminated with a continuous laser sheet (Quantum Excel Laser, 2 W, 532nm) and filmed at 1000fps (Fastcam Photron 1024 PCI). Further information can be found in supplementary Fig. S3.

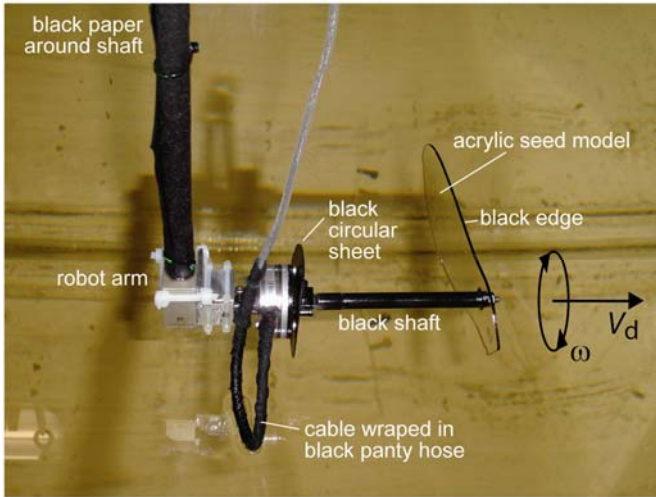
**Spinner experiments in air.** To verify that our flat plate models of autorotating seeds were reasonably accurate, we compared the LEVs generated by an *Acer pseudo-platanus* L. seed with thin 1:1 scale balsa wood models. We found that balsa models that were  $\leq 4\%$  thick generated similar LEVs as those created by real seeds under kinematically identical conditions. This comparison shows that our 3-4% thick acrylic models used in our DPIV study were thin enough to capture the aerodynamic behavior of real seeds. Further information can be found in supplementary Fig. S6,7.

**Calculation seed flight performance.** We calculated the aerodynamic descent performance of various seeds using a basic point mass performance analysis derived in Equation S1.

**Movie S1. LEV visualization near the base of a freely flying *Acer pseudo-platanus* L.**

The movie shows a leading edge vortex that is stably attached near the base of a freely flying maple seed (*Acer pseudo-platanus* L.). The seed is spinning at stationary height in a vertical wind tunnel and the flow is visualized at different spanwise stations using a laser light sheet. The laser light sheet illuminates the motion of smoke particles dispersed in the air around the wing that trace the airflow (see methods in Fig. S3). The seed has a small horizontal speed and, therefore, the seed flies slowly out of the laser sheet. As a result the local airflow is visualized at successively more outward spanwise stations of the spinning seed. Key frames from this illustrative movie are shown in Fig. S5, where we further discuss the structure of this leading edge vortex.

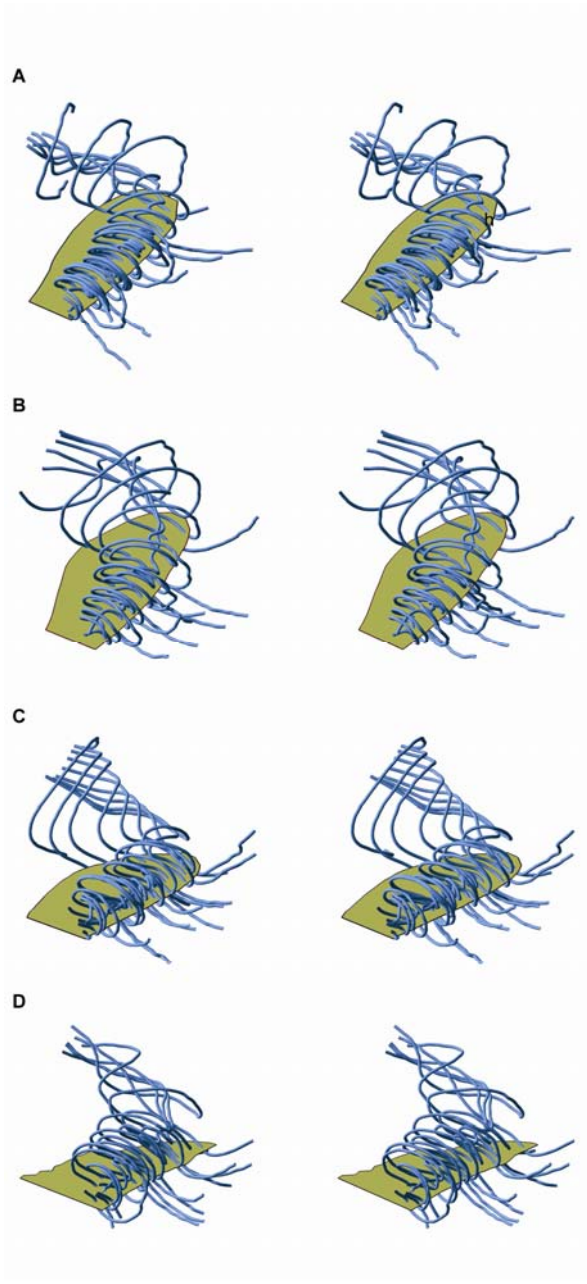
**Figure S1. Dynamically scaled Robot model of a descending autorotating seed**



**Robot.** The robot seed consists of an acrylic model driven by a translating robot arm (S1). The robot can only translate horizontally, thus to simulate the descending flight of the hornbeam and maple seeds we tilted the flight path by  $90^\circ$ . The acrylic seed models were fixed to the shaft at their measured cone and pitch angle (S2). We revolved ( $\omega$ ; angular velocity) and translated ( $V_d$ ; descent speed) the model seeds in oil such that they followed the same path at the same Reynolds number as seeds in air (S2). The model seed moves from left to right such that it flies in undisturbed oil; the wake of the seed hits the arm (and not *vice versa*).

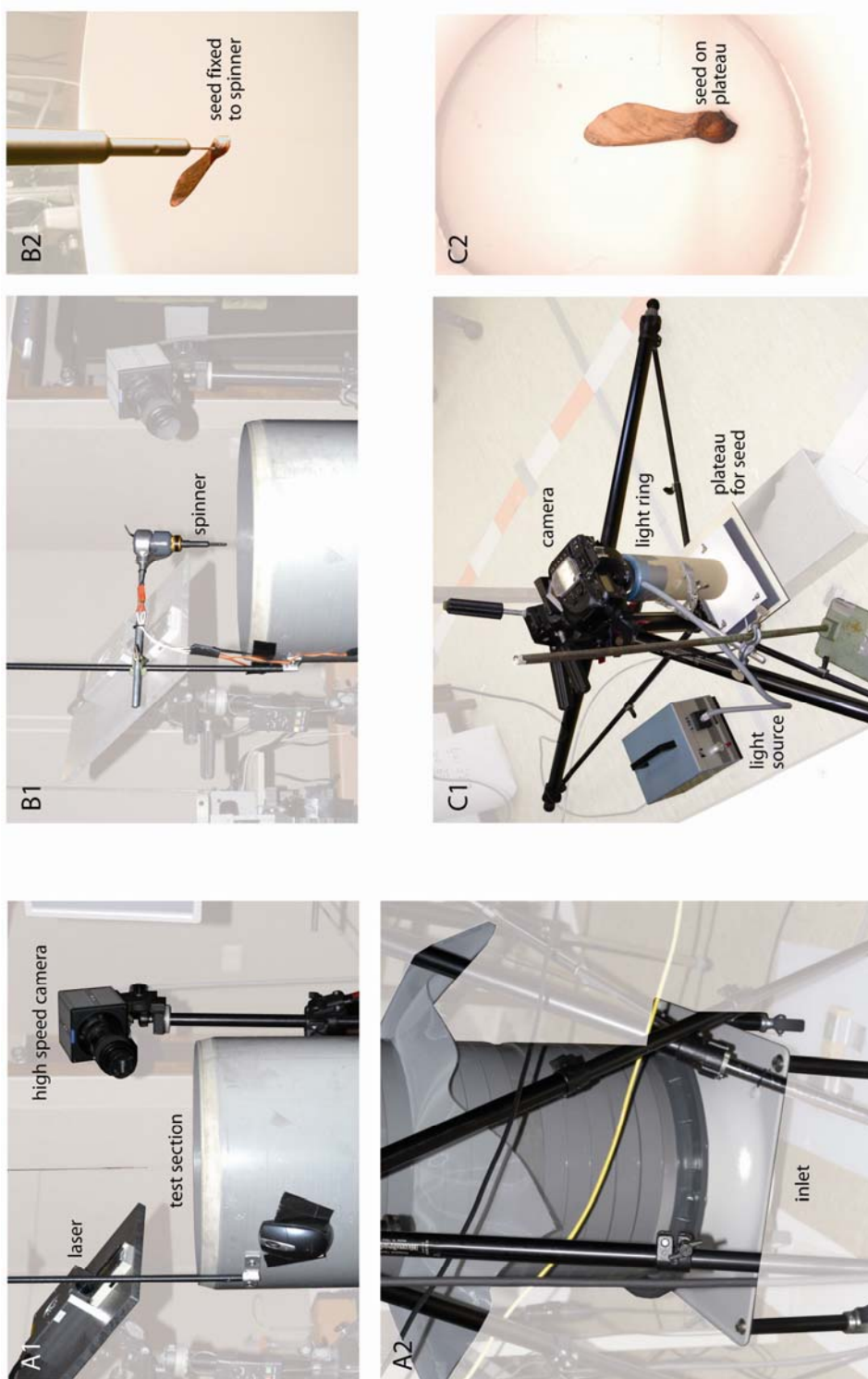
**DPIV.** We measured the three-dimensional flow field using a stereo Digital Particle Image Velocimetry setup described previously (S5). The laser light sheet was oriented parallel to chord length, (close to the one shown) and was activated using an automated trigger. To minimize laser light reflections in our DPIV image, both the shaft and edges of the wings were painted black. In addition, we placed a black circular sheet in front to shield the robot's knuckle, wrapped the sensor cable in black panty hose (Sheer Energy, Leggs), and wrapped a black sheet around the shaft of the robot arm.

Figure S2. Stereo images of the LEV measured on seed models



Stereo images of the large leading edge vortex (LEV) measured for all four model seeds. (**A-D**) Flow visualization of absolute (in lab frame) streamlines, calculated from the three-dimensional velocity field measured using DPIV. The models of the three maple seeds (**A**, *m1*; **B**, *m2*; **C**, *m3*) and the hornbeam seed (**D**, *h*) generate a LEV with significant spanwise flow that is connected to the tip vortex. The angle of attack of the seed increases from (**A**) to (**D**). Note that the seed spins clockwise (in all figures). (view point & angle are identical in A-D, stereo angle offset is  $\pm 3.5$  degrees)

Figure S3. Free flight LEV visualization setup based on a vertical wind tunnel.



We designed a vertical wind tunnel to study the flow and kinematics of freely flying maple seeds as well as model seeds, and a spinner to examine the flows created by real seeds and model seeds rotating with prescribed kinematics.

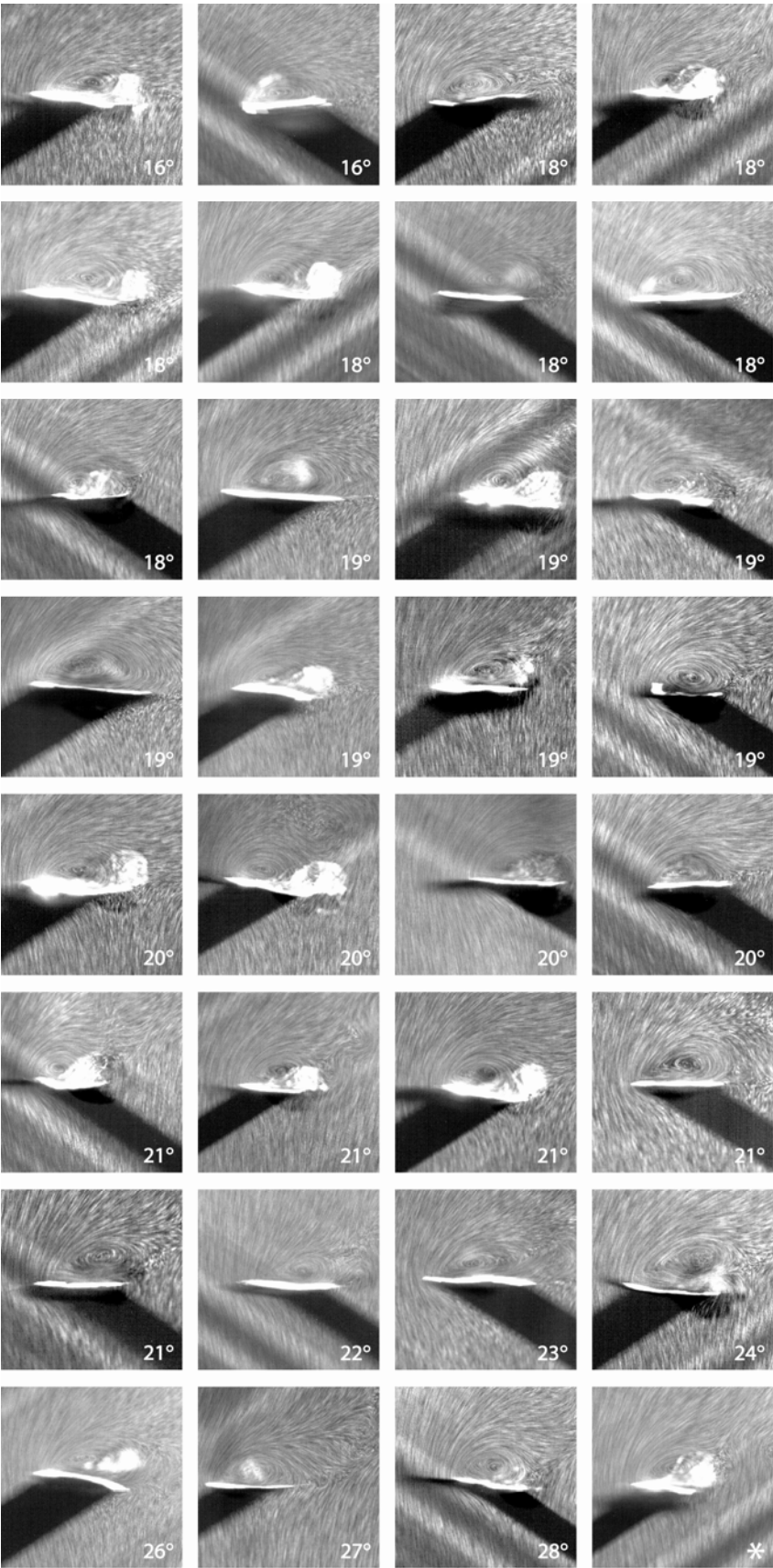
(**A1-A2**) The vertical wind tunnel has an open test section with a diameter of 400 mm in which the maximum air speed is approximately 2 m/s. Wind speed was measured using a hotwire anemometer (Testo 405-V1). The fan of the wind tunnel (Rucon ARA61-400-4E with a rounded inlet) is integrated in the inlet of the tunnel (**A2**).

Behind the fan we placed flow straighteners to improve the flow quality: 7 gauzes after the fan to straighten the flow to a large extent and make it uniform, then a honey comb with a length diameter ratio of 10, and finally 2 additional gauzes. To visualize the flow we filled the complete room with smoke using a smoke generator (HQ POWER VDP900HZ) with high density smoke fluid. We illuminated the smoke particles in a light sheet above the wing using a 2W continuous laser (Quantum Excel Laser, 532 nm) and filmed their movement at 1000 Hz using a digital high speed camera (Fastcam Photron 1024 PCI) equipped with a macro lens (AF Micro NIKKOR 105 mm 1:2.8 lens) (**A1**). In interpreting the flow, please note that the incoming smoke particles have an upward velocity and get a horizontal velocity component due to the rotational motion of the seed, which flies at a stationary height above the wind tunnel.

(**B1-2**) We designed a spinner setup with which we could rotate both real seeds and models thereof. This setup allowed us to look at the effect of geometry on aerodynamics without having to precisely match the center of gravity and inertia tensor of the models with the real seeds, which would be required for free flight comparison. Furthermore, in a free flight comparison between autorotating seeds and models it would be challenging to fly both seed and model at similar cone and pitch angles. Finally, comparing the flow at identical spanwise stations between seeds and their models in free flight is cumbersome due to the movements of the seed in the horizontal plane during free flight. For all these reasons we decided to compare a freely flying seed, with a real seed and a model seed attached to the spinner at the same air speed and angular velocity. (**B2**).

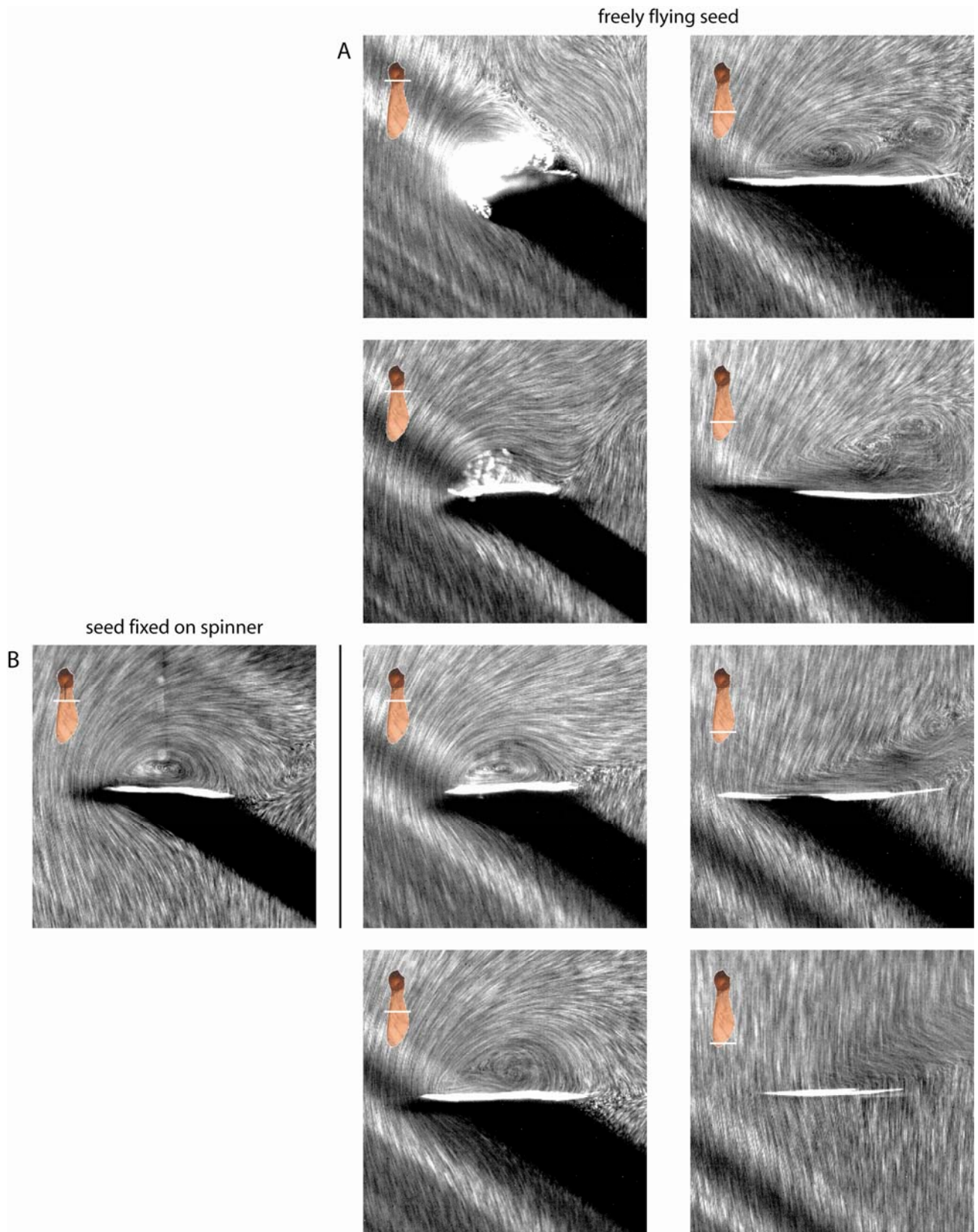
(**C1-2**) To measure the wing surface area of our freely flying seeds we photographed them while they were lying on a platform (we used a suction hole underneath to fix them). A sample photograph (D700 NIKON Camera with a AF NIKKOR 35-70 mm lens) is shown in **C2**. We measured the mass of the seeds using an electronic balance (Ohaus Adventurer Pro AV114CU, accuracy 0.1 mg). All seeds were painted black using a permanent marker to minimize the scatter of laser light. The ink was applied on both sides of the seed in rapid succession to eliminate deformation due to asymmetric drying. The small amount of ink increased the weight of the seed by 1.3% on average.

Figure S4. LEV visualization near the base of 32 freely flying *Acer pseudo-platanus* L. seeds



Free flight LEV visualization of 32 maple seed specimens (*Acer pseudo-platanus* L.) for a spanwise station close to the base (exact location unknown). The specimens were collected on the 26<sup>th</sup> of September 2008 from four branches of a maple tree (*Acer pseudo-platanus* L.) that grows near the Department of the Animal Sciences of Wageningen University. On this day several seeds flew out of the tree due to wind and would detach when a branch was vibrated. We collected many seeds, which we subdivided in four groups: green vs. dried and intact vs. hollow seeds (hollow due to worms). All the dried and intact seeds were stored in closed containers in a refrigerator. We used a random number generator (custom programmed using Matlab 2007a, The MathWorks) to select 103 out of 233 specimens for testing in our apparatus. The weight distribution of this collection of 103 specimens had two peaks, which turned out to be due to underdevelopment of the embryo in 47 specimens (This could be visually determined after dissecting some individuals which reassured us that a deformed, shrunken, and thin nut is under developed). We flight tested the heavier 56 seeds with well-developed embryos in our wind tunnel. Of these 56 specimens 34 flew stably enough in our tunnel for flow visualization (others flew straight out of the test section due to slow, but unstable, side wards motion). The flow visualization was sufficient to verify the presence of a LEV near the base in the 32 cases depicted in this figure (in two out of 34 experiments we were unable to visualize the flow near the base). In all except the last case, we were able to measure the advance ratio of the seed, which we used to calculate the angle of attack at the wingtip (written in the lower right corner of each image). For these freely flying seeds we did not correct the angle of attack at the wing tip for pitch angle, which is typically of the order of 1 degree (see paper) and therefore difficult to measure during flow visualization. The angle of attack due to advance ratio was used to order the LEV visualizations from low to high angle of attack. Because the exact spanwise station at which we visualized the LEV is not known and varies for every seed, we can only coarsely observe the trend that the size of the LEV increases with angle of attack. Also note that the camera position varies for every seed: in some cases we see the flow slightly from behind or from the front of the seed, instead of purely spanwise. The wide range of angles of attack and wing loadings at which these maple seeds operate illustrate the remarkable robustness of the LEV near the base of the wing of maple seeds.

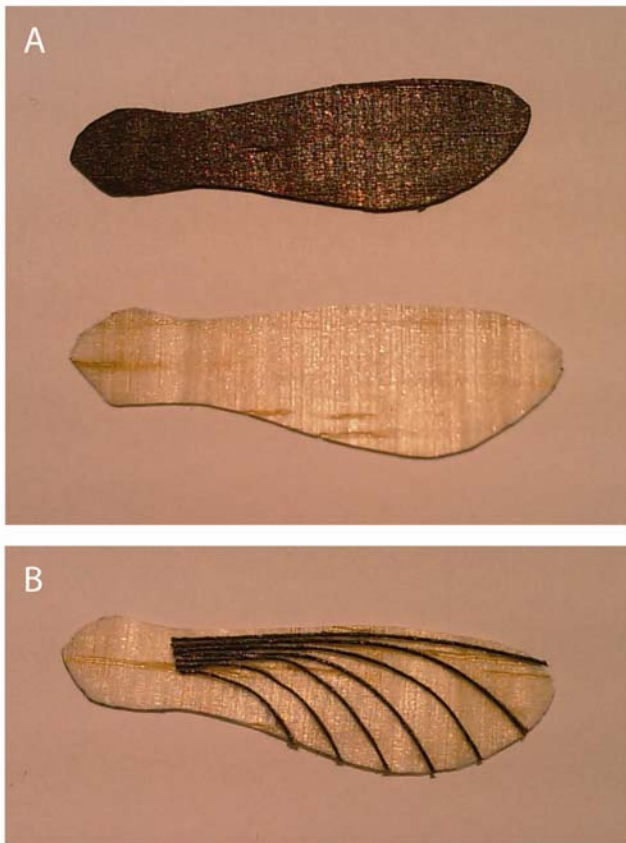
Figure S5. Spanwise variation in cordwise flow of a freely flying *Acer pseudo-platanus* L.



(A) Flow visualization during free flight around an *Acer pseudo-platanus* L. specimen at eight successively more outward spanwise stations. Due to the sideward motion of the seed with respect to the stationary light sheet we were able to film the flow starting at the base and for every revolution at a further outward spanwise station. The

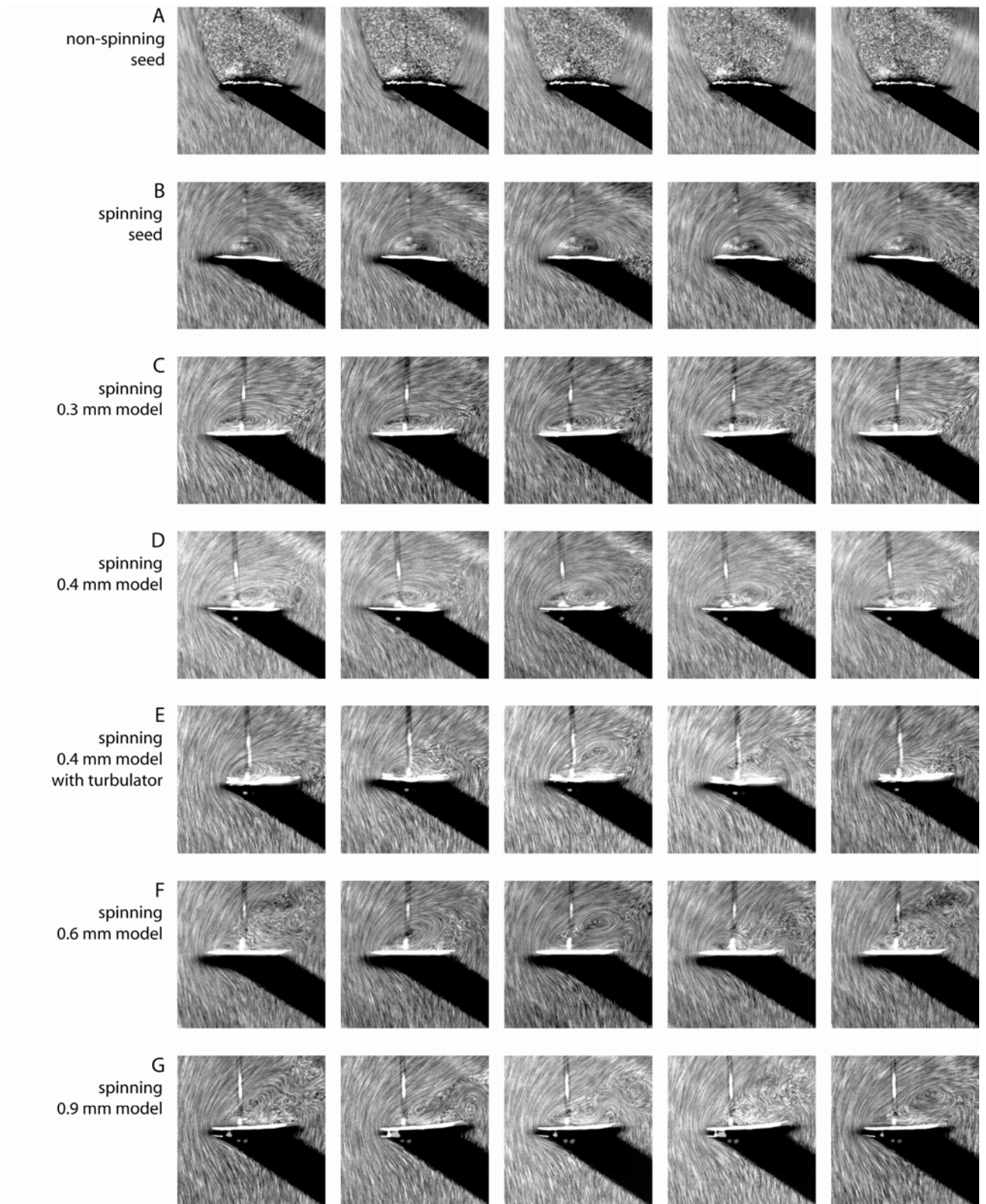
movie sequence is provided in Supplementary Movie M1. As for other seeds we observed a stably attached LEV near the base, which starts to become unstable and unsteady at roughly  $\frac{1}{2}$  of the seed's span (upper right image, see also Supplementary Movie, M1). At this spanwise station we often observed double leading edge vortices that separate from the wing at different stages. A qualitatively similar bifurcation of the LEV into double LEVs has been observed on the upper surface of flapping insect wings at similar Reynolds numbers of order 1000 (S6). The average Reynolds number at which the *Acer pseudo-platanus* L. maple seeds (*m4*) we tested operate is 2700, which is significantly higher than the 1700 (*m1*), 1200 (*m2*) and 650 (*m3*) of the other maple seed species we studied using the robot model. The much higher Reynolds number, and corresponding flow effects, for *m4* is therefore the most parsimonious explanation for the found differences in LEV structure in the wingtip-region between seeds that operate at moderate (*m1-3*) versus high Reynolds number (*m4*). **(B)** We found that the flow around the freely flying specimen **(A)** is qualitatively similar to the flow around the same specimen fixed to a spinner at roughly the same spanwise station ( $\sim 30\%$  span w.r.t. the center of rotation). This can be observed by comparing the image left of the black vertical line (seed pinned to spinner) with the image immediately to its right (same seed freely flying). We mounted the seed by hand at similar pitch and cone angle, operating it at the same angular velocity and air speed as the freely flying seed.

**Figure S6. Balsa wood models of *Acer pseudo-platanus* L.**



(A) To test if the simplified geometry of our dynamically-scaled model seeds affect the generation of the LEV we compared the flow generated by seeds and balsa models with variable thickness and surface morphology. The models were made out of high quality balsa wood sheets (C-grain for chord-wise stiffness) with smooth surface finishing. The thickness of these sheets ranged from 0.3, 0.4, 0.6 to 0.9 mm, which corresponds with 4.1, 5.5, 8.3, 12.4 % thickness with respect to the average chord length. The planform of the models is based on the seed shown in Fig. S5. All models were painted black similar to the real seeds (see the caption of Fig. S3C). (B) To test the effect of basic turbulators on the formation and stability of the LEV, we mounted 0.20–0.25 mm thin cyanoacrylate reinforced threads (infused small amount of cyanoacrylate) on a 0.4 mm thick balsa model. The pattern of the added turbulators is coarsely based on the roughness pattern of the freely flying seed in Fig. S5.

**Figure S7. Flow visualization at 30% span of *Acer pseudo-platanus* L. and various balsa models**



We tested the effect of seed morphology on the formation and stability of the LEV by comparing real seeds with balsa wood models in air. The models are based on the morphology of the freely flying specimen in Fig. 5A. The average relative thickness of the dynamically scaled models in oil are ( $m1$ , 3.9%;  $m2$ , 3.7%;  $m3$ , 3.7%;  $b$ , 3.3%), slightly thinner than our thinnest balsa model (0.3 mm; 4.1%, see Fig. S6). The results of our flow visualizations

at 30% radius (with respect to the center of rotation) for various kinematic and morphological models at five successive rotational periods (identical to the free flight period) are shown in rows A through G. **(A)** The non spinning seed fixed to a pin at the same vertical air speed encountered during free flight generates a large wake with a completely separated flow. **(B)** Spinning the seed at the correct free flight angular velocity and vertical air speed (same as in A) has a profound effect on the flow field, which now separates at the leading edge and re-attaches at the trailing edge to form a prominent LEV. **(C)** A 0.3 mm (4.1% thick) balsa wood model also generates a prominent stable leading edge vortex as found in (B). The extent of vortex above the seed seems less in C compared to B, suggesting an effect of the simplified morphology, but the qualitative flow pattern is very similar. **(D)** The 0.4 mm thick model generates a slightly bigger LEV, which is however slightly unsteady. **(E)** Adding 0.2 mm thick turbulators to the model did not stabilize the LEV, it rather becomes less steady and looks more similar to the one generated by the 0.6 mm model and less similar to the one generated by the real seed in (B). The turbulators have a relative thickness of 2.7%, which is quite thick, however the boundary layer thickness on the upper side of the seed is clearly even thicker. Further study is required to test if more subtle turbulator morphology would have a positive effect. **(F,G)** The 0.6 and 0.9 mm thick balsa models generate even less stable LEVs which do not resemble the LEV of the seed in (B).

Based on this study we conclude that our thin (<4% thick) dynamically scaled model seeds made out of acrylic sheet model the seed reasonably well, because our 4.1% thick balsa model is able to generate qualitatively the same flow pattern as the real seed: a stable and pronounced LEV.

### Supplementary Equations. Relating descent time to wing loading and aerodynamic efficacy

We relate seed descent time to its wing loading and aerodynamic efficacy using a basic point performance analysis (S7) and the blade element method. The blade element method is applied similarly to the one used in calculating forward insect flight performance (S8). The vertical aerodynamic force generated by a seed counteracts its weight  $W$ . The vertical force distribution over the wing can be integrated along the span using small chord wise surface segments of chord wise length  $c$  and width  $dr$  at radial distance  $r$  (Fig. 1). The total vertical force  $F_V$  can be calculated as follows:

$$F_V = \int_0^R C_v(r) \times 1/2 \rho (V_d^2 + \omega^2 r^2) \times c(r) dr, \quad (S1)$$

in which  $C_v$  is the vertical force coefficient,  $\rho$  the density,  $V_d$  the descent speed and  $\omega$  the angular velocity and, finally, ' $r$ ' indicates that the particular variable depends on radius. Noting that  $F_V$  is equal (in magnitude) to the seed's weight  $W$ , which is equal to mass  $m$  times gravity constant  $g$ . We can now define the average vertical force coefficient as follows:

$$C_{v,ave} = \frac{mg}{\int_0^R 1/2 \rho (V_d^2 + \omega^2 r^2) \times c(r) dr} = \frac{mg}{1/2 \rho (V_d^2 + \omega^2 R_g^2) S} = \frac{W}{1/2 \rho \left(1 + \frac{1}{k_g^2}\right) V_d^2 S}, \quad (S2)$$

in which  $R_g$  is the radius of gyration of the seeds wing and  $k_g$  the advance ratio at the radius of gyration of the seed:

$$k_g = \frac{V_d}{\omega R_g}. \quad (S3)$$

We now find the following expression for the descent time per meter height for a seed of given mass and wing area in air ( $\rho=1.23$ ) on earth ( $g=9.81$ ):

$$T = \frac{1}{V_d} = \sqrt{\frac{1/2 \rho \left(1 + \frac{1}{k_g^2}\right) C_{v,ave} S}{W}} = \sqrt{\frac{0.61 D F}{W/S}}, \quad (S4)$$

in this the non-dimensional number  $DF$  represents the aerodynamic efficacy of the seed, which captures the combined effect of advance ratio and vertical force coefficient on descent time, whereas wing loading  $W/S$  is dimensional and shows how descent time scales with size. Based on Eq. S4 we can now look into the factors through which a seed can maximize its descent time per meter height at a given wing loading: The seed can increase its average vertical force coefficient  $C_{V,ave}$  through optimizing wing morphology and the angle of attack of the wing (S7). Angle of attack depends, however, directly on advance ratio  $k_g$ . (Fig. 1D) which therefore determines  $C_{V,ave}$ . We therefore need to include both  $C_{V,ave}$  and  $k_g$  simultaneously in the descent factor  $DF$ , because the expression that builds up the descent factor should be maximized as a whole, which we derive based on Eqn. S4:

$$DF = \left(1 + \frac{1}{k_g^2}\right) C_{V,ave} = \frac{2W}{\rho V_d^2 S}, \quad (S5)$$

The descent factor represents a dimensionless number for the aerodynamic efficacy of the seed of a given wing loading  $W/S$ , analogous to the climb factor for gliders, but extended to the larger glide angles at the radius of gyration of seeds that do not allow us to assume  $1 + \frac{1}{k_g^2} \approx \frac{1}{k_g^2}$ , which is typically done for gliders, because their descent speed is much smaller than forward speed (S7).  $DF$  is a measure of aerodynamic efficacy, because the gravitational power input required for the descent of the seed (descent speed times weight) goes down with the inverse of the square root of descent factor. To evaluate the aerodynamic efficacy ( $DF$ ) of a seed with a given wing loading we can now simply calculate its descent factor based on readily available field and lab data ( $W$ ,  $S$  and  $V_d$ ) and Equation S5. Formula S4 and S5 also work for seeds that spin along two axes or simply glide (gliding is in our analysis equivalent to autorotating with an infinite radius of curvature of the path along which the seed's radius of gyration moves). For straying seeds we consider the average descent time per meter height calculated (by definition) using the time-averaged descent and forward speed, yielding Equations similar to S4 and S5, but time averaged:

$$\langle T \rangle = \sqrt{\frac{0.61}{W/S}} \langle \sqrt{DF} \rangle, \quad (S6)$$

$$\langle \sqrt{DF} \rangle^2 = \frac{2W}{\rho \langle V_d \rangle^2 S}, \quad (S7)$$

We used these Equations S4-S7 to show how descent time scales with the inverse square root of wing loading times the square root of the descent factor. This we use to illustrate in Fig. 5 that the descent time of autorotating seeds cannot be predicted based on scaling the descent time of gliding and straying seeds to the higher wing loadings of autorotating seeds: The autorotating seeds descend much longer for a particular wing loading, which corresponds with significantly higher descent factors and, therefore, higher aerodynamic efficacy.

## References

- S1. Dickson, W.B. & Dickinson, M.H. The effect of advance ratio on the aerodynamics of revolving wings. *J. Exp. Biol.* **207**, 4269-4281 (2004).
- S2. Azuma, A. & Yasuda, K. Flight performance of rotary seeds. *J. Theor. Biol.* **138**, 23-53 (1989).
- S3. Yasuda, K. & Azuma, A. The autorotation boundary in the flight of samaras. *J. Theor. Biol.* **185**, 313-320 (1997).
- S4. Dickinson, M.H., Lehmann, F.-O. & Sane, S.P. Wing rotation and the aerodynamic basis of insect flight. *Science* **284**, 1954 -1960 (1999).
- S5. Poelma, C., Dickson, W.B. & Dickinson, M.H. Time-resolved reconstruction of the full velocity field around a dynamically-scaled flapping wing. *Exp. Fluids* **41**, 213-225 (2006).
- S6. Lu, Y., Shen, G.X. & Lai, G.J. Dual leading-edge vortices on flapping wings. *J. Exp. Biol.* **209**, 5005 -5016 (2006).
- S7. Ruijgrok, G.J.J. *Elements of airplane performance*. Delft University Press Delft (1994).
- S8. Dickson, W.B. & Dickinson, M.H. The effect of advance ratio on the aerodynamics of revolving wings. *J. Exp. Biol.* **207**, 4269-4281 (2004).